ELECTROCHEMISTRY

Ultrastable supported oxygen evolution electrocatalyst formed by ripening-induced embedding

Wenjuan Shi[1]†‡, Tonghao Shen[2]†, Chengkun Xing[1], Kai Sun[1], Qisheng Yan[1], Wenzhe Niu[1], Xiao Yang[1], Jingjing Li[1], Chenyang Wei[1], Ruijie Wang[1], Shuqing Fu[1], Yong Yang[1], Liangyao Xue[1], Junfeng Chen[1], Shiwen Cui[1], Xiaoyue Hu[1], Ke Xie[3], Xin Xu[2,4]*, Sai Duan[2]*, Yifei Xu[1]*, Bo Zhang[1]*

The future deployment of terawatt-scale proton exchange membrane water electrolyzer (PEMWE) technology necessitates development of an efficient oxygen evolution catalyst with low cost and long lifetime. Currently, the stability of the most active iridium (Ir) catalysts is impaired by dissolution, redeposition, detachment, and agglomeration of Ir species. Here we present a ripening-induced embedding strategy that securely embeds the Ir catalyst in a cerium oxide support. Cryogenic electron tomography and all-atom kinetic Monte Carlo simulations reveal that synchronizing the growth rate of the support with the nucleation rate of Ir, regulated by sonication, is pivotal for successful synthesis. A PEMWE using this catalyst achieves a cell voltage of 1.72 volts at a current density of 3 amperes per square centimeter with an Ir loading of just 0.3 milligrams per square centimeter and a voltage degradation rate of 1.33 microvolts per hour, as demonstrated by a 6000-hour accelerated aging test.

Water electrolysis can convert electricity harvested from renewable but intermittent solar or wind energy into "green" (i.e., environmentally sustainable) hydrogen (1). Large-scale and cost-effective generation of green hydrogen is considered a key to the future clean energy industry with net-zero carbon emissions (2). Presently, the proton exchange membrane water electrolyzer (PEMWE) stands out as the most promising technology for green hydrogen production owing to its high current density, rapid system response, and low gas crossover rate (3, 4). Central to the functioning of PEMWE is the anodic oxygen evolution reaction (OER), which provides the protons and electrons needed for PEMWE. Enhancement in the activity and stability of OER catalysts has a deep impact on the overall efficiency and economic viability of the device (5, 6). Iridium oxide (IrO_x) is so far the only practical OER catalyst that can work continuously in PEMWE (7). Nevertheless, the high cost [>$180 per gram (8)] and scarce reserve [only 3×10^{-6} parts per million in Earth's crust (9)] of Ir pose substantial barriers to the future terawatt-scale deployment of PEMWE (10).

To enhance the activity and stability of the catalyst while reducing the Ir content, various approaches have been explored, such as alloying (11, 12) and compositing with perovskites (13–15) or mixed oxides (16, 17). An efficient and commonly used strategy is loading IrO_x nanoparticles (NPs) with high surface areas onto different supports, typically metal oxides (18–24). Activities of the resultant supported catalysts are often comparable to or even superior to that of pure IrO_x, owing to the strong catalyst-support interactions that tune the electronic structure of Ir and its adsorption energy to OER intermediates (22, 24). This strategy has led to PEMWE performance improvements, realizing cell voltages of <1.9 V at a current density of 2 A cm^{-2} with Ir loading of <0.5 mg cm^{-2} (23, 24). Nonetheless, the primary challenge confronting the supported catalysts is stability; even the best reported results for cell voltage degradation rate with Ir loading of <0.5 mg cm^{-2} remains ~100 μV hour^{-1} (23, 24), which is about 50 times too high as compared with the ambitious 2.3 μV hour^{-1} target set by the United States Department of Energy (DOE) for the year 2026 (25).

It has been demonstrated that the primary causes for the instability of the aforementioned supported catalysts are the dissolution, redeposition, detachment, and agglomeration of the IrO_x NPs (18, 21, 26). The dissolution and redeposition issues could be mitigated by suppressing the overoxidation of Ir through electron donation from metal oxide supports, as observed for many oxides with rich oxygen vacancies, such as antimony-doped tin oxide (18),

TaO_x (24), and CeO_x (27, 28). Intuitively, a solution to the problems of detachment and aggregation would be to firmly anchor the working Ir sites into the supports. A recent advance in this direction has entailed the atomic loading of Ir^{VI} sites into MnO_2 through oxidative ligand substitution, achieving <1 μV hour^{-1} potential degradation in PEMWE. However, the cell voltage at a current density of 3 A cm^{-2} was 1.88 V, 80 mV higher than the DOE 2026 target, which compromises the desired activity (29). The gap in activity is probably due to the low amount of loaded Ir^{VI} owing to the requirement of complete ligand replacement, limiting the number of available active sites and thus curtailing the catalyst's performance. Consequently, finding a catalyst that can fulfill all DOE 2026 targets continues to represent an unresolved pursuit for PEMWE.

In this work, we integrated the advantages of high-density Ir sites per unit area offered by NPs with the stability imparted by anchoring the working catalyst on metal oxide supports. We developed a ripening-induced embedding (RIE) strategy to securely embed IrO_x NPs into CeO_x support. Extra sonication processes were adopted to ensure matchable rates between support growth and Ir nucleation, leading to an ultrastable and efficient catalyst characterized by embedding depths optimally at half of the particle diameter. PEMWE based on this RIE catalyst can attain a cell voltage of 1.72 V at a current density of 3 A cm^{-2} with a voltage degradation rate of 1.33 μV hour^{-1}, and the total platinum group metal (PGM) loading (both anode and cathode) is 0.4 mg cm^{-2}, satisfying all DOE 2026 targets. Furthermore, this RIE strategy has proven versatile in extensions to other combinations of metal NPs and metal oxides that exhibit increased stability as effective catalysts under different reaction conditions, thereby charting a distinct path in the design of highly resilient catalyst systems.

Design of the RIE strategy

We conceived of a strategy to securely embed the working catalysts into supports by initiating the formation of Ir NPs directly on the surface of the growing support. Practically, this RIE strategy is accomplished through a polyol method (30), where an iridium salt is reduced into monodispersed Ir NPs and loaded onto the metal oxide support by heating in ethylene glycol. In this protocol, the applied heating facilitates the growth of the unaged support particles through Ostwald ripening (31), making the embedding possible.

A successful RIE process, however, requires a fast ripening of the support, to match the rapid nucleation of the Ir NPs. According to the theorem of Lifshitz and Slyozov (32), in a diffusion-controlled scenario, the growth rate of ripening particles is proportional to their surface energy. In other words, the supports with higher

Fig. 1. Schematic illustration of the embedding strategy. Identical parameters of Ir NP nucleations are applied to the KMC simulations on the growth of the (111) and (211) surfaces of metal oxide supports (MO_x).
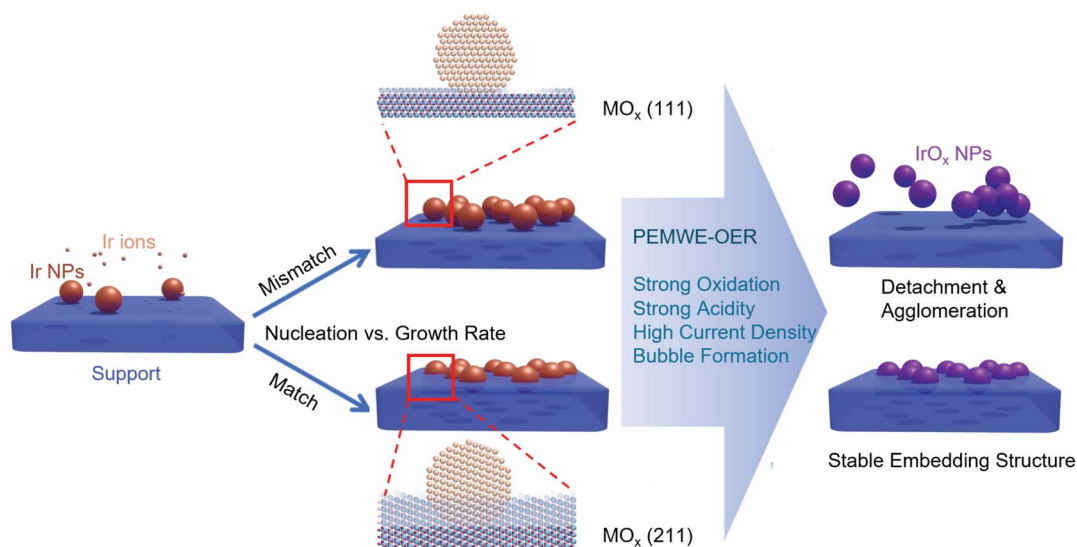
surface energies are expected to exhibit a faster increase of their average sizes. Indeed, preliminary simulations using density function theory (DFT)–based kinetic Monte Carlo (KMC) affirm this expectation (Fig. 1 and table S1). Specifically, stable facets, such as the (111) surface of a face-centered cubic metal oxide support, exhibit only submonolayer growth in a reasonable synthesis time of a few hours, which is inadequate for embedding the fast-nucleating NPs. In contrast, high-energy facets such as the (211) surface grow faster, resulting in a successful embedding of the Ir NPs during the synthesis process. Under the PEMWE-OER condition, these Ir NPs are rapidly oxidized into IrO_x. During this process, the lattice constant would be increased, and the Ir dissolution would be suppressed by electron donation from the support, such as the aforementioned CeO_x (27), resulting in a net expansion of the NPs and enhancing their anchoring in the support. In light of these considerations, it is imperative that the growth rate of high-energy facets of the support be both fast and sustainable, aligning with the rapid nucleation rate of Ir NPs, to successfully synthesize the intended embedded catalysts.

Experimental synthesis of supported catalysts with RIE

We applied a sonication-assisted polyol method to promote the growth of the high-energy facets by first synthesizing sub-10-nm CeO_x particles with rough surface morphology. Sonication created a transient (<1 ms) (33) local high temperature (5000 to 5500 K, as indicated by sonoluminescence spectra; see fig. S1) (34) upon the collapse of acoustic cavitation bubbles. This intense heat, along with local high pressure, shock wave, and other effects, can erode the surface of CeO_x and facilitate the exposure of high energy facets (35, 36). Moreover, carbon substrate was used to facilitate the dis-
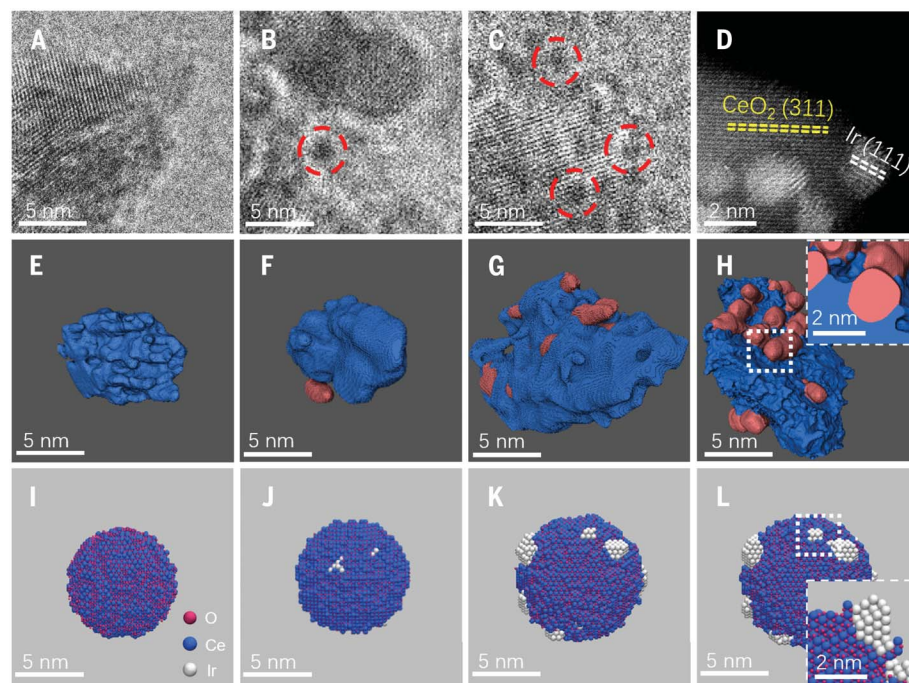
persion of CeO_x, which was removed at the end of synthesis by calcination in air (figs. S2 to S5 and tables S2 and S3) (37). The size of the as-synthesized CeO_x NPs ranged from 4 to 10 nm, averaging 7.9 ± 1.3 nm (Fig. 2A and fig. S2), in line with the broad peaks in the x-ray diffraction spectrum (see figs. S6 to S8 for detailed characterizations). According to the Ostwald ripening theorem, smaller particles dissolve and recondense onto larger ones (31). Our intentionally broad size distribution of CeO_x was

thus expected to amplify the driving force for ripening. Electron tomography (ET; Fig. 2E and movie S1) confirmed the rough morphology of CeO_x, which should further enhance the growth rate as predicted by the theorem of Lifshitz and Slyozov (32).

Subsequently, Ir NPs were nucleated onto the prepared CeO_x support particles using the polyol method. Regrettably, no desired embedding was observed in the product (figs. S9 to S15), implying an imbalance between the

Fig. 2. Formation process of supported catalysts with RIE. (**A** to **C**) (Cryo-)TEM images of the CeO_x support particles after 0, 5, and 60 min of Ir loading, respectively, with Ir NPs highlighted by dashed red circles. (**D**) Cs-corrected HAADF-STEM images of CeO_x after 180 min of Ir loading. (**E** to **H**) (Cryo-)ET reconstructed 3D models of the samples shown in (A) to (D). CeO_x and Ir NPs are colored in blue and pink, respectively. Inset of (H) shows the cross section of the area in the box. (**I** to **L**) KMC simulation of the formation process of RIE-Ir/CeO_x at time points corresponding to (A) to (D).

CeO_x growth kinetics and the fast nucleation of Ir NPs. Indeed, closer scrutiny of the synthesis process uncovered that Ir nucleation reached completion within the first hour, whereas the CeO_x ripening process persisted even after 3 hours (fig. S22). This finding underscored the necessity to further accelerate the growth rate of the support.

To address this challenge, sonication was reintroduced during the Ir loading process, which was expected to expedite the dissolution of smaller particles and accelerate the ripening process. In this scenario, it was found that the ripening rate of the CeO_x support was tripled by sonication (figs. S16 to S22). Cryo–transmission electron microscopy (cryo-TEM) and cryo–electron tomography (cryo-ET) were used to monitor the synthesis process. These techniques permit high-resolution three-dimensional (3D) imaging of solution samples without drying or washing (38, 39), which is essential for accurately studying the Ir nucleation and embedding kinetics (see discussions in figs. S15 and S16). Cryo-TEM revealed that a few Ir NPs were deposited on the roughened CeO_x support after 5 min of reaction (Fig. 2B, dashed red circle; also in movie S2). At this initial stage, the cryo-ET image confirmed that the Ir NPs were not yet embedded into the CeO_x support (Fig. 2F), with the particle size of CeO_x remaining virtually unchanged (fig. S18). In the hours that followed, more Ir NPs nucleated onto the CeO_x surface (Fig. 2C, dashed red circles), with the particle size of CeO_x expanding to 10.4 ± 1.1 nm (fig. S20). Notably, the Ir NPs were embedded into the CeO_x support, as clearly shown in the cryo-ET 3D reconstruction (Fig. 2G; see also movie S3), reaching an embedding depth of ~1.0 nm, nearly equivalent to the expanded radius of CeO_x. Although most of the ripening process was complete within the first hour (fig. S22), the reaction was prolonged to 3 hours to optimize the embedding process. The final product, designated RIE-Ir/CeO_x, was examined by spherical aberration–corrected scanning TEM (Cs-corrected STEM). The high-angle annular dark field (HAADF) image (Fig. 2D) illustrates clearly the embedding of Ir NPs into the CeO_x lattice to a depth of ~1 nm, occurring indiscriminately across crystallographic orientations. The embedding was further corroborated by the cross section of the ET results (Fig. 2H; see also movie S4).

As illustrated in Fig. 2, the ripening rate of the support is proportional to its surface energy, and a high support surface energy is essential for the successful execution of the RIE process. To exemplify this point, a control experiment was conducted using ~30-nm commercial CeO_2 crystallites as the support. These crystallites predominantly expose well-defined and thermodynamically stable (111) facets (fig. S23; see detailed characterizations in figs. S6 to S8) (40). Ir NPs were then nucleated onto these crystallites using the same sonication-assisted polyol method for 3 hours. The final product, namely C-Ir/CeO_2 (fig. S28; see also movie S5), was detected, where no embedding was observed, and the average size of the CeO_2 crystallites remained largely unchanged (figs. S24 to S28). Moreover, we also measured the size of CeO_x before and after heating and sonication without Ir loading. A similar level of particle growth was observed (fig. S29 and table S3), confirming that the ripening of the CeO_x is not affected by Ir loading.

The mechanisms underlying the RIE process were further investigated using KMC simulations on top of DFT calculations (fig. S30), a powerful approach enabling atomic-scale simulations of crystallization phenomena over hours-long timescales (41). A random removal of surface atoms was applied to the surface of CeO_x during the simulations, to mimic the surface erosion caused by sonication. The KMC simulation results excellently reproduced the growth and embedding processes during synthesis (Fig. 2, I to L; see also figs. S31 to S33). Further theoretical analysis revealed that the growth rate of the CeO_x support was profoundly influenced by the concentration of CeO_x species released by surface erosion, which accelerated the ripening of CeO_x and facilitated the Ir NP embedding. Moreover, the rough morphology of CeO_x, dominated by high-energy surfaces, sustained a higher concentration of CeO_x in solution and fostered a rapid species exchange with solution, thereby amplifying the ripening rate, a phenomenon that is in line with the Lifshitz and Slyozov theorem (32). Indeed, inductively coupled plasma mass spectrometry (ICP-MS) confirmed that the concentration of Ce species in solution was increased upon sonication (table S5). In contrast, the simulated growth rate of a CeO_2 crystallite consisting of stable (111) facets was very slow even with sonication, confirming its incapacity to embed Ir NPs (figs. S28C, S34, and S35 and table S4), again in good agreement with the experimental observations.

PEMWE performance of the supported RIE catalyst

The electrical and proton conductivities of RIE-Ir/CeO_x were measured to be 0.893 and 0.010 S cm^{-1} (figs. S36 to S39 and tables S6 to S8), respectively, which allow its use in the PEMWE devices with high current densities (42, 43). The OER catalytic activity and stability of RIE-Ir/CeO_x were then assessed under practical working conditions in a PEMWE, using an anode with 0.3 mg cm^{-2} of Ir loading complemented by a cathode with 0.1 mg cm^{-2} of platinum (Pt) loading. Polarization curves verified the heightened OER activity of the catalyst, achieving a cell voltage of 1.72 V at a 3 A cm^{-2} current density (Fig. 3A), accompanied by ~99 and ~98% Faraday efficiencies for H$_2$ and O$_2$ generation, respectively (figs. S40 and S41). This performance not only exceeded C-Ir/CeO_2 and commercial IrO$_2$ but also surpassed the corresponding DOE 2026 target (1.8 V at 3 A cm^{-2}), suggesting a higher mass activity of RIE-Ir/CeO_x, considering its lower Ir content (15.6 wt %; table S9) than that of C-Ir/CeO_2 (17.2 wt %) and commercial IrO$_2$ (87.7 wt %). Using a quasi–membrane electrode assembly method (figs. S42 and S43), the mass activity of RIE-Ir/CeO_x at 3 A cm^{-2} was quantified at 777.4 A g$_{Ir}^{-1}$ (fig. S44 and table S10), representing a 6.32-fold increase over C-Ir/CeO_2 (122.9 A g$_{Ir}^{-1}$) and a 17.04-fold improvement compared with commercial IrO$_2$ (45.6 A g$_{Ir}^{-1}$) operating at equivalent potentials. After normalization with surface areas determined by the Brunauer-Emmett-Teller method or electrochemical active surface area, the specific activity of RIE-Ir/CeO_x maintained its superiority over both C-Ir/CeO_2 and commercial IrO$_2$ (figs. S45 to S47). Comparable enhancements in activity have been reported for other Ir-based supported catalysts, attributed to Ir-support electronic interactions (18, 28), although not to such a large extent, hinting at a more profound interaction facilitation in the case of RIE-Ir/CeO_x.

The long-term stability of the catalyst in PEMWE-OER was tested in an accelerated aging experiment that lasted for >6000 hours (Fig. 3C), with the current density stepped up from 1 A cm^{-2} to 8 A cm^{-2} and then reverted to 2 A cm^{-2}. The flat plateaus at each current density signify the exceptional stability of the RIE-Ir/CeO_x catalyst across a wide range of the current density in PEMWE. Notably, the cell voltage at 2 A cm^{-2} remained virtually unchanged from the commencement to the termination of the experiment, while the decay rate at 3 A cm^{-2} was evaluated to be 1.33 µV hour^{-1} (table S18). In contrast, the control catalyst C-Ir/CeO_2 exhibited a much higher voltage decay rate of 3.1 mV hour^{-1} during the 1 A cm^{-2} to 8 A cm^{-2} aging test (fig. S48). Marked disparities were also observed in constant current density tests, where a 200 mV voltage increase occurred within 800 hours at 1 A cm^{-2} (Fig. 3C, inset) or 30 hours at 8 A cm^{-2} (Fig. 3B). We also tested the performance of CeO_x loaded with Ir by only heating, and it also cannot work stably at 1 A cm^{-2} (fig. S49). These results strongly suggest that the exceptionally high stability of the RIE catalyst can be ascribed to the distinctive embedding structure, which effectively prevents the detachment and agglomeration of Ir NPs, as initially hypothesized (Fig. 1). TEM images, taken before and after the 8 A cm^{-2} constant current density test, clearly demonstrate the well-preserved embedding structure in RIE-Ir/CeO_x, contrasting starkly with the evident NP detachment and aggregation in C-Ir/CeO_2 (Fig. 3B, insets; see also figs. S50 and S51). Inhibition of Ir dissolution and detachment in
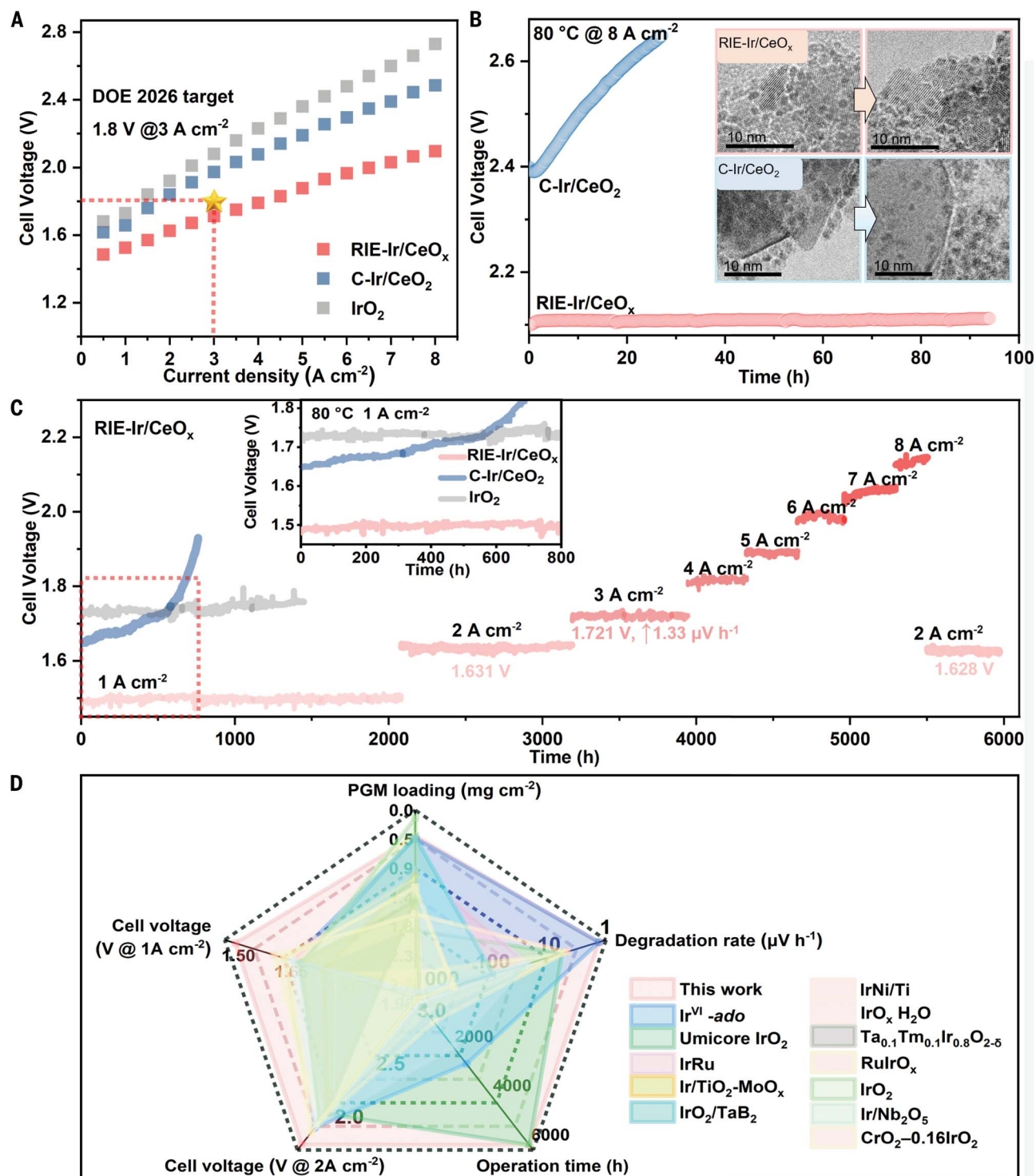
Fig. 3. PEMWE performances of the supported RIE catalyst. (**A**) Polarization curves of the PEMWE. (**B**) Chronopotentiometric curves of the PEMWE using RIE-Ir/CeO$_x$ and C-Ir/CeO$_2$ catalysts operated at 8 A cm^{-2}. The inset shows TEM images of the catalysts taken before and after the operation. (**C**) Chronopotentiometric curves of the PEMWE using RIE-Ir/CeO$_x$ catalyst at a sequential current density of 1, 2, 3, 4, 5, 6, 7, 8, and 2 A cm^{-2}. Inset shows chronopotentiometry curves using RIE-Ir/CeO$_x$, C-Ir/CeO$_2$, and IrO$_2$ catalysts operated at 1 A cm^{-2}, respectively. (**D**) Comparisons between RIE-Ir/CeO$_x$ and other Ir-based PEMWE-OER catalysts.

RIE-Ir/CeO$_x$ was further validated by ICP-MS measurements (figs. S52 to S54 and tables S11 and S12), where the physical confinement of the embedded structure and electron donation effect of CeO$_x$ may both make important

contributions (see detailed characterizations in figs. S55 to S68 and tables S14 and S15). The NP size in RIE-Ir/CeO$_x$ expanded from 2.2 ± 0.1 nm to 2.3 ± 0.3 nm. This expansion is logically attributed to the aforementioned oxida-

tion of Ir to IrO$_x$ (Fig. 2), a transformation that is beneficial to the stability of the embedding structure, as anticipated.

As stated above, the RIE-Ir/CeO$_x$ displays high cell activity (1.72 V at 3 A cm^{-2}) and stability

Fig. 4. Reliability and extensibility of the RIE catalysts.
(**A**) Chronopotentiometric curves of 10 different PEMWE devices using RIE-Ir/CeO$_x$ catalyst, at a sequential current density of 1, 3, 4, and 8 A cm^{-2}. The curves are plotted in 10 different colors. (**B** and **E**) TEM images of RIE-Ir/ZrO$_x$ and RIE-Pt/CeO$_x$. Insets show ET reconstructed 3D models. Different materials are labeled as follows: ZrO$_x$, purple; CeO$_x$, blue; Ir, pink; and Pt, yellow. (**C** and **F**) TEM images of C-Ir/ZrO$_2$ and C-Pt/CeO$_2$. (**D**) PEMWE chronopotentiometric curves operated at 2 A cm^{-2}, using RIE-Ir/ZrO$_x$ or C-Ir/ZrO$_2$ as the anode catalysts, and commercial Pt/C as the cathode catalyst, respectively. (**G**) PEMWE chronopotentiometric curves operated at 2 A cm^{-2}, using RIE-Pt/CeO$_x$ or C-Pt/CeO$_2$ as the cathode catalysts, and RIE-Ir/CeO$_x$ as the anode catalyst, respectively.
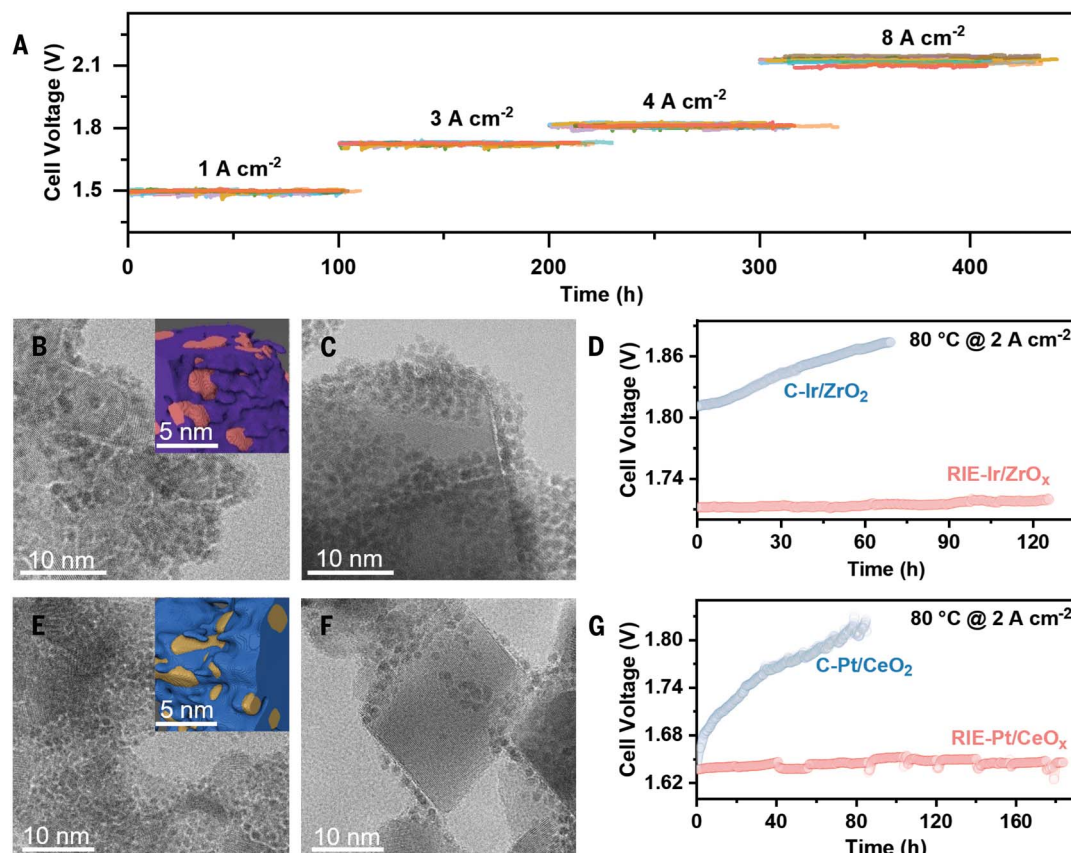
(potential degradation rate of 1.33 μV hour^{-1}) with a low PGM loading (0.4 mg cm^{-2}). This performance satisfies the stringent DOE 2026 targets of cell activity (1.8 V at 3 A cm^{-2}), potential degradation rate (2.3 μV hour^{-1}), and total PGM content (0.5 mg cm^{-2}) for a single PEMWE device. Notably, the potential degradation rate already meets the DOE's ultimate target (2.0 μV hour^{-1}) (*25*), guaranteeing >10 years of catalyst lifetime (table S13). The performance of RIE-Ir/CeO$_x$ was compared with other state-of-the-art Ir-based PEMWE-OER catalysts (Fig. 3D) (*17, 22–24, 29, 44–50*), clearly showing the superior overall performance of the catalyst. The potential degradation rate of the RIE catalyst is lower than most of the other Ir-based catalysts, including commercial IrO$_2$ (Umicore). Very recently, a <1.0 μV hour^{-1} PEMWE potential degradation rate was reported for atomically dispersed Ir^{VI} oxide (table S16) (*29*), using between 0.38 and 0.48 g cm^{-2} of PGM loaded onto a Nafion 115 membrane (active area of 1 cm^2), but the cell activity (1.88 V at 3 A cm^{-2}) did not meet the DOE 2026 target. All these comparisons highlight the advantage of RIE-Ir/CeO$_x$ in balancing activity, stability, and cost.

Reliability and extensibility of the RIE catalysts

The reliability of the RIE-Ir/CeO$_x$ catalyst was tested on 10 different PEMWE devices (Fig. 4A),

confirming its catalytic activity and stability at different current densities (figs. S69 to S74 and tables S17 and S18). As the RIE strategy does not rely on a certain element or compound, it can be used to enhance the activity and stability for other combinations of metal and metal oxide supported catalysts. The performances of these catalysts in the anode OER and cathode hydrogen evolution reaction (HER) of PEMWE, as well as hydrogen generation from NaBH$_4$ hydrolysis, were tested. ZrO$_x$ (fig. S75A), another Earth-abundant metal oxide, was used as the support for OER in PEMWE. The RIE-Ir/ZrO$_x$ (Fig. 4B) displays enhanced stability in comparison with the unembedded control sample (Fig. 4, C and D). Probably because of the weaker electron donation ability of ZrO$_x$, its activity is not as impressive as that of RIE-Ir/CeO$_x$. For the cathode in PEMWE, the effective HER catalyst is Pt. In this case, the RIE-Pt/CeO$_x$ was found to display a higher stability as well (Fig. 4, E to G), showing again that the embedding structure can stabilize the supported catalyst under rapid bubble flushing. Similar results were observed for a completely different combination from the above catalysts, that is, RIE-Ru/TiO$_2$ (fig. S75B), for catalyzing NaBH$_4$ hydrolysis (fig. S76). All these examples demonstrate that the RIE strategy can efficiently enhance the stability of supported catalysts in harsh conditions with rapid bubble formation, showing the broad adaptability of our method.

Conclusions

This work has successfully tackled the stability challenge faced by the supported PEMWE-OER Ir catalyst through the development of a straightforward yet effective RIE strategy. This approach prevents the detachment and agglomeration of Ir NPs by synchronizing the ripening rate of the support with the nucleation rate of Ir. This was achieved by using sonication to generate CeO$_x$ particles with rough surfaces and further accelerate their ripening by enhancing the dissolution of the smaller particles. The resultant RIE-Ir/CeO$_x$ not only meets the DOE 2026 targets of activity and Ir loading but also attains DOE's ultimate goal of unparalleled stability, marking a milestone in the development of PEMWE-OER catalysts. The relatively low price of CeO$_x$ ($1740 per metric ton) (*51*) allows the large-scale deployment of the catalyst in the future. Furthermore, the RIE strategy can be extended to other catalyst systems, which paves the way for designing the next generation of supported catalysts with superior stabilities.

REFERENCES AND NOTES

1. A. Ursua, L. M. Gandia, P. Sanchis, *Proc. IEEE* **100**, 410–426 (2012).
2. A. M. Oliveira, R. R. Beswick, Y. Yan, *Curr. Opin. Chem. Eng.* **33**, 100701 (2021).
3. M. Carmo, D. L. Fritz, J. Mergel, D. Stolten, *Int. J. Hydrogen Energy* **38**, 4901–4934 (2013).
4. S. Shiva Kumar, V. Himabindu, *Mater. Sci. Energy Technol.* **2**, 442–454 (2019).

5. S. Wang, A. Lu, C.-J. Zhong, *Nano Converg.* **8**, 4 (2021).
6. J. Song *et al.*, *Chem. Soc. Rev.* **49**, 2196–2214 (2020).
7. C. Wang, L. Feng, *Energy Adv.* **3**, 14–29 (2024).
8. Strategic Metals Invest, Iridium prices; https://strategicmetalsinvest.com/iridium-prices/.
9. C. Minke, M. Suermann, B. Bensmann, R. Hanke-Rauschenbach, *Int. J. Hydrogen Energy* **46**, 23581–23590 (2021).
10. M. A. Hubert, L. A. King, T. F. Jaramillo, *ACS Energy Lett.* **7**, 17–23 (2021).
11. Y. Zhao *et al.*, *Nano Energy* **59**, 146–153 (2019).
12. Y.-T. Kim *et al.*, *Nat. Commun.* **8**, 1449 (2017).
13. L. C. Seitz *et al.*, *Science* **353**, 1011–1014 (2016).
14. O. Diaz-Morales *et al.*, *Nat. Commun.* **7**, 12363 (2016).
15. Y. Chen *et al.*, *Nat. Commun.* **10**, 572 (2019).
16. F. Zhao *et al.*, *J. Am. Chem. Soc.* **143**, 15616–15623 (2021).
17. S. Hao *et al.*, *Nat. Nanotechnol.* **16**, 1371–1377 (2021).
18. H.-S. Oh *et al.*, *J. Am. Chem. Soc.* **138**, 12552–12563 (2016).
19. E. Oakton *et al.*, *ACS Catal.* **7**, 2346–2352 (2017).
20. H. Ohno, S. Nohara, K. Kakinuma, M. Uchida, H. Uchida, *Catalysts* **9**, 74 (2019).
21. F. Claudel *et al.*, *ACS Catal.* **9**, 4688–4698 (2019).
22. Z. Shi *et al.*, *Angew. Chem. Int. Ed.* **61**, e202212341 (2022).
23. S. Ge *et al.*, *Energy Environ. Sci.* **16**, 3734–3742 (2023).
24. Y. Wang *et al.*, *Nat. Commun.* **14**, 5119 (2023).
25. United States Department of Energy, Technical targets for proton exchange membrane electrolysis; https://www.energy.gov/eere/fuelcells/technical-targets-proton-exchange-membrane-electrolysis/.
26. H. Yu, L. Bonville, J. Jankovic, R. Maric, *Appl. Catal. B* **260**, 118194 (2020).
27. W. Gou *et al.*, *Nano Energy* **104**, 107960 (2022).
28. Z. Dong *et al.*, *Adv. Funct. Mater.* **34**, 2400809 (2024).
29. A. Li *et al.*, *Science* **384**, 666–670 (2024).
30. F. Bonet *et al.*, *Nanostruct. Mater.* **11**, 1277–1284 (1999).
31. W. Ostwald, *Z. Phys. Chem.* **22U**, 289–330 (1897).
32. I. M. Lifshitz, V. V. Slyozov, *J. Phys. Chem. Solids* **19**, 35–50 (1961).
33. D. Sunartio, M. Ashokkumar, F. Grieser, *J. Am. Chem. Soc.* **129**, 6031–6036 (2007).
34. K. S. Suslick, E. B. Flint, *Nature* **330**, 553–555 (1987).
35. H. Wang *et al.*, *Phys. Chem. Chem. Phys.* **4**, 3794–3799 (2002).
36. D. G. Shchukin, E. Skorb, V. Belova, H. Möhwald, *Adv. Mater.* **23**, 1922–1934 (2011).
37. W. Shi, A-H. Park, H.-U. Park, Y.-U. Kwon, *J. Catal.* **384**, 22–29 (2020).
38. Y. Zhu *et al.*, *Adv. Mater.* **35**, e2301549 (2023).
39. P. Zhang, H. Du, S. Cui, P. Zhou, Y. Xu, *Responsive Mater.* **1**, e20230025 (2023).
40. J. Conesa, *Surf. Sci.* **339**, 337–352 (1995).
41. M. Kotrla, *Comput. Phys. Commun.* **97**, 82–100 (1996).
42. M. Bernt *et al.*, *J. Electrochem. Soc.* **168**, 084513 (2021).
43. L. Chen, Q. Xu, S. Z. Oener, K. Fabrizio, S. W. Boettcher, *Nat. Commun.* **13**, 3846 (2022).
44. L. Tao *et al.*, *Joule* **8**, 450–460 (2024).
45. E.-J. Kim *et al.*, *Appl. Catal. B* **280**, 119433 (2021).
46. K.-R. Yeo, K.-S. Lee, H. Kim, J. Lee, S.-K. Kim, *Energy Environ. Sci.* **15**, 3449–3461 (2022).
47. J. Xu *et al.*, *Sci. Adv.* **9**, eadh1718 (2023).
48. K. J. Choi, S.-K. Kim, *Int. J. Hydrogen Energy* **48**, 849–863 (2023).
49. S. Siracusano, V. Baglio, N. Van Dijk, L. Merlo, A. S. Aricò, *Appl. Energy* **192**, 477–489 (2017).
50. W. J. Shi *et al.*, Ultrastable supported oxygen evolution electrocatalyst formed by ripening-induced embedding, Dryad (2024); https://doi.org/10.5061/dryad.dr7sqvb7g.
51. Statista, Cerium oxide price worldwide from 2009 to 2020 with a forecast from 2021 to 2030; https://www.statista.com/statistics/450146/global-reo-cerium-oxide-price-forecast/.

ACKNOWLEDGMENTS

SUPPLEMENTARY MATERIALS